Computational Materials Science 219 (2023) 112005

Contents lists available at ScienceDirect

Computational Materials Science

journal homepage: www.elsevier.com/locate/commatsci

Full Length Article

Emergent failure transition of pearlitic steel at extremely high strain rates

Lun-Wei Liang [a,b,c], Shi-Cheng Dai [a,c], Yan Chen [a,c], Hai-Ying Wang [a,c], Yun-Jiang Wang [a,c,*], Lan-Hong Dai [a,c,d,*]

[a] State Key Laboratory of Nonlinear Mechanics, Institute of Mechanics, Chinese Academy of Sciences, Beijing 100190, PR China
[b] Sany Automobile Manufacturing Co. Ltd., Changsha 410100, PR China
[c] School of Engineering Science, University of Chinese Academy of Sciences, Beijing 101408, PR China
[d] School of Future Technology, University of Chinese Academy of Sciences, Beijing 101408, PR China

ARTICLE INFO

Keywords:
Pearlitic steels
Fracture
Crack
Dislocation nucleation
Molecular dynamics

ABSTRACT

It is a common wisdom that metallic materials become brittle once being deformed quickly. However, here we reveal an abnormal strain-rate-induced brittle-ductile-delamination transition in a widely used pearlitic steel with unique structure of alternative arrangement of nanoscale ductile ferrite and brittle cementite through extensive molecular dynamics simulations. In contrast to the brittle cleavage fracture in conventional crystalline alloys, the brittle fracture in pearlitic steel at relatively low strain rate is mediated by the nanoscale cavitation ahead of crack tip, akin to the widely observed fracture mode in metallic glasses. As the strain rate increases, fracture mode transforms to a dislocation nucleation mediated ductile mechanism. At extremely high strain rate, it is found that the fracture mode turns to be collective delamination at the interfaces, leading to a surprising "delamination toughening". The abnormal brittle-to-ductile transition with increasing deformation rate is physically rationalized by a mechanistic model, which is based on a scenario of energetic competition between the interface cleavage and the dislocation nucleation in the vicinity of crack tip. Once the strain rate exceeds a critical value, fracture transitions to dislocation nucleation dominated. When strain rate increases to extremely high values, there is no enough time for either crack propagation or dislocation nucleation, and the collective delamination of interfaces occurs which involves only instantaneous bond breaking at weakly bonded regions, i.e. the interface. The unravelled phenomenon challenges the conventional knowledge of materials deformation and failure which might shed light on coordinating unanticipated utilities of the ultrastrong pearlitic steels in extreme environments.

1. Introduction

Cold-drawn pearlitic steel wires, consisting of alternative nanoscale ductile ferrite and brittle cementite layers, are widely used as engineering structural materials because of a good combination of ultrahigh strength and appropriate tensile ductility [1–3]. Some components made from pearlitic steels are inevitably subjected to high loading rate in defense and civil applications, such as steel wires in arresting system, tower cranes, and mine hoist. There are many studies on the failure and deformation behaviors of metallic materials at relatively low loading rates [4–6]. However, experimental strain rates in metals can even up to about 10^{12} s^{-1} under extreme loading conditions [7,8]. High rate deformation usually transforms structural materials to be brittle even though they are ductile at ambient conditions, which is detrimental to their durability in service [9]. Therefore, there is always a pressing necessity to find structural materials without catastrophic failure at severe loading conditions. The failure mode of materials under high deformation rate is a result of ductile *versus* brittle mechanical competition. Crack-tip dislocation nucleation is also a very important issue as a usual blunting mechanism of crack, which is critical to understand the ductile *versus* brittle behavior of solid materials [10–16]. In many cases, the brittle-to-ductile response is mainly controlled by the competition between dislocation emission and cleavage decohesion of adjacent atomic planes at crack tip. Dislocation emission near crack tip shields the crack from the external stress field, and thus results in the crack blunting [16–19]. Recently, some studies pointed out that dislocation activity controls the two-step brittle-to-ductile transitions in pearlitic steels, in which they focused on the temperature effect on fracture behaviors [20,21]. It is noted that both dislocation emission and cleavage are a rate-dependent process. However, there is rare report on the

* Corresponding authors at: State Key Laboratory of Nonlinear Mechanics, Institute of Mechanics, Chinese Academy of Sciences, Beijing 100190, PR China.
E-mail addresses: yjwang@imech.ac.cn (Y.-J. Wang), lhdai@lnm.imech.ac.cn (L.-H. Dai).

https://doi.org/10.1016/j.commatsci.2022.112005
Received 1 July 2022; Received in revised form 14 October 2022; Accepted 23 December 2022
Available online 9 January 2023

influence of strain rate on the brittle *versus* ductile behaviors of the nanolamellar pearlitic steel wires, which is a more engineeringly relevant loading condition rather than thermal fluctuation.

Better understanding of the fracture mechanisms – especially at atomic-scale – is of significant importance to design materials with desired fracture toughness, which is the key to avoid catastrophic failure in service. Cold-drawn pearlitic steel exhibits unique nanoscale lamellar architecture, which is the structural origin of its superior mechanical properties. In such a lamellar texture, the ferrite-cementite interfaces plays a critical role in the mechanical properties – strength, ductility, fracture toughness, and work hardening – of the pearlitic steels [22,23]. The interface can be simultaneously served as dislocation source (with interfacial misfit dislocation as embryo) and sink, which both hinders dislocation motion and allows partial slip transfer from ferrite to cementite [24–26]. It is the microscopic mechanism underlying the strategy of increasing strength of pearlitic steel by reducing lamellar spacing [2,3,27,28] without compromising too much tensile ductility. However, it is still a challenging task to conduct *in situ* observation of the atomic-scale mechanisms of bond breaking and dislocation initiation processes due to the limitations in spatial–temporal resolutions of even the mostly advanced characterization techniques. On the other hand, atomistic simulations such as molecular dynamics (MD) with accurate empirical potential can deal with these problems and have been utilized extensively to explore the deformation and fracture mechanism of the ferrite-cementite interface [24–26,29–32].

For the ferrite-cementite interface, previous atomistic simulations are mainly concentrated on the energetics and dislocation morphology in versatile interfaces with different orientations between ferrite and cementite, as well as the plastic deformation mechanisms in the case of either monotonic or cyclic loadings [24,26,29]. It has been found that the interfacial energies and structures depend strongly on both the chemistry and registry of the interface [29]. More interestingly, the ferrite-cementite interface acts as both sources and sinks of dislocation which renders both high yield stress and reasonable ductility [33], in analogy to the role of twin boundary in nanotwinned metals [34–37]. Upon loading, either dislocations nucleate from the ferrite-cementite interface, or slip transfer from ferrite to cementite across the interface, which is unfavorable to pearlite, in particular, in the case of fatigue which acquires final damage in cementite [26]. In light of these atomic-scale information obtained from MD simulations, it was also suggested that higher ductility of the cold-drawn pearlitic steels can be obtained by controlling the interfacial dislocation spacing [24].

In the case of common Fe-C alloys or steels, there are plenty of MD simulations on the fracture behaviors demonstrated by atomistic cracking models in body-centered cubic (BCC) iron (α-Fe), which is a matrix phase of pearlite, under mode I crack loading. For example, Guo *et al.* [38,39] investigated the mechanism of low-temperature fracture at the crack tip in α-Fe, and they found that successive emission of dislocations at the crack tip induces phase transformation from BCC to close-packed hexagonal structures. Möller *et al.* [40] compared the fracture behaviors (cleavage, dislocation emission, and twinning) of different crack systems in α-Fe with different EAM potentials. Partial dislocations at the crack tip lead to the occurrence of planar faults. Wang *et al.* [41] found that the ductile shear slips in α-Fe are activated near the crack tip in the quasi-cleavage process, and dislocation motions occur at the beginning stage of crack propagation. Ersland *et al.* [42] demonstrated that the changes in the crack geometry during loading encourages dislocation emission instead of the unstable crack growth. Gordon *et al.* [43] have made an attempt to explore the dislocation activation pathway for α-Fe from the crack tip using the nudged elastic band (NEB) method [44]. It is found that higher stress leads to lower activation energy for dislocation nucleation and thus promotes ductility. They also suggested that the structural heterogeneity is another key factor in facilitating ductile dislocation emission. Some other simulations have provided atomistic insight into fracture involving the interaction between grain boundary and crack [45,46]. Dislocation has been found to prefer nucleation at a certain distance along the grain boundary in front of the crack tip [45]. All the reported MD simulations have brought about meaningful understandings of the microscopic fracture processes in the generic iron and steels. However, there is missing investigation on the effect of loading rate on the brittle or ductile fracture of the ferrite-cementite steel, which is a necessity for structural application in severe environments.

In the present work, extensive MD simulations are conducted to investigate the fracture mechanisms in the nanoscale ferrite-cementite cold-drawn pearlitic steel under mode I crack loading scheme, with particular interest in the effect of deformation rate on the fracture mode. Section 2 describes the atomistic model and calculation details. Section 3 demonstrates the mechanical response, fracture behaviors, and mechanisms of failure at different strain rates. An unexpected brittle-ductile-delamination transition is discovered. Section 4 discusses the possible mechanism of the brittle-ductile-delamination transition. Finally, we summarize the results in Section 5.

2. Methodology

2.1. Model setup and molecular dynamics

MD simulations are performed using the open-source LAMMPS package [47]. Three potentials (MEAM [48], Tersoff [49], and EAM [50]) are recently verified to be suitable for the studying deformation behaviors of the ferrite-cementite interface in pearlite via atomistic simulations. The three empirical potentials produce the same interfacial orthogonal dislocation structure and slip transfer across the ferrite-cementite interface of pearlite [24,25,51]. In the literature, the MEAM potential has been widely used to study the deformation mechanisms associated with the interface in pearlite [24–26]. We use the MEAM potential [48] to describe the force field in pearlitic steels. It is an extension to the original EAM [50] potential to include the directionality of chemical bonding, which enables accurate prediction of properties of BCC Fe and metallic-covalent materials [24], in particular, the mechanical properties such as elastic constants, interfacial energies etc. that are closely relevant to the simulation of plastic deformation and fracture of the ferrite-cementite system. As reported in our previous work [52], the calculated lattice parameters of orthorhombic cementite are $a = 4.47$ Å, $b = 5.09$ Å, and $c = 6.67$ Å, respectively. The BCC Fe has a calculated lattice parameter of $a = 2.85$ Å. These calculated parameters are very close to the experimental values [53].

While there is consensus that a single pearlite colony exhibits a single consistent orientation relationship (OR) in the lamellae, this OR is not the same for all the pearlite colonies, as several of them have been experimentally observed [53,54]. However, there is no consensus as to which of the three ORs is the most favorable one. Among the five orientation relationships between ferrite and cementite reported in pearlitic steels up to date, the Bagaryatskii orientation relationship [55] is probably the most widely studied circumstance due to its high degree of registry [25,26,51] Obeying the convention $a \leq b \leq c$ for the crystallographic directions of the cementite unit cell, the Bagaryatskii orientation relationship is expressed as:

$$[100]_{\theta} || [1\bar{1}0]_{\alpha}$$

$$[010]_{\hat{1}_{,}} || [110]_{\hat{1}\pm}$$

$$(001)_{\hat{1}_{,}} || (11\bar{2})_{\hat{1}\pm}$$

in which the subscripts $\hat{1}_{,}$ and $\hat{1}\pm$ denote cementite and ferrite, respectively.

Plenty of experiments demonstrate a very strong anisotropy of the fracture behavior in pearlitic steels. The catastrophic failure have been found in the longitudinal direction of the nanostructured pearlitic steel wires [56,57]. The crack path in pearlitic steel wires is identified to be

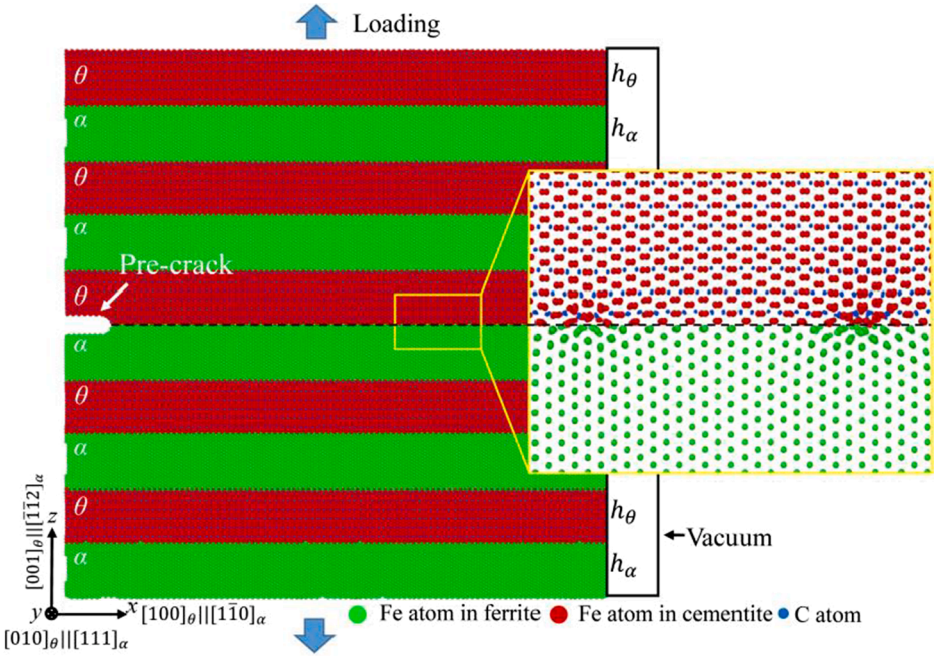

Fig. 1. Atomic model of the mode I crack of the ferrite-cementite interface. The crack growth direction is parallel to the drawing direction, i.e. $[1\bar{1}0]_\alpha$ or $[100]_\theta$. Î ± and Î¸ indicate ferrite and cementite, respectively.

along the interface between ferritic and the carbon-rich (formerly cementite) phases [58]. In the present simulations, we consider a representative mode I crack model with the crack growth direction parallel to the drawing direction (⟨1 1 0⟩ fiber texture in ferrite), as shown in Fig. 1. The dimension of the crack sample is $L_x \times L_y \times L_z = 45.7 \times 15.8 \times 41.1$ nm^3 (about 2.5 million atoms) oriented along the principal x: $[100]_{\hat{I}_\alpha} \| [1\bar{1}0]_\alpha$, y: $[010]_{\hat{I}_\alpha} \| [111]_\alpha$, and z: $[001]_{\hat{I}_\alpha} \| [\bar{1}\bar{1}2]_\alpha$ axes. Although, it is quite computational time-consuming for the present MEAM potential, the results are more reliable compared with conventional EAM or Tersoff potentials [50,59]. The in-plane dimensions are designed to be sufficiently large to properly reduce the initial strain between ferrite and cementite due to lattice incoherence. The strains in x and y directions are ~ 0.13% and ~ 0.18% before relaxation, respectively, which is acceptable to produce a reasonable atomistic model for interface. Owing to the fact that the plastic mechanisms remains unchanged once the layer thickness ratio varies [24], only a case with ratio 1:1 of the ferrite to cementite phase is considered in order to save computational cost. A pre-crack with half length a_0 and notch radius r is created on the ferrite-cementite interface. The crack is introduced by removing a few layers of atoms, resembling the crack cut by the focused ion beam technique in real experiment. The terminating plane of the cementite at the crack surface keeps a Fe-FeC type to maintain the structural consistency with the ferrite-cementite interface. The interface structure and energy with different terminating planes within cementite plane have been characterized systematically by using atomistic simulations recently by Guziewski *et al.* [51]. The interfacial energy with different terminating planes is very close to each other as demonstrated in our previous work [52] and in Ref. [51]. For the interface structure, it has been found to be composed of a rectangular network of interfacial dislocations for the Bagaryatskii orientation relationship. This interfacial dislocation structure remains unchanged regardless of the terminating planes within cementite phase that forms the interface. The dislocation type and spacing remains constant with respect to change in the terminating plane, but the dislocation height and width at the ferrite-cementite interface are different [51]. The terminating plane of the cementite at the crack surface keeps a Fe-FeC type to maintain the structural consistency with the ferrite-cementite interface. The cutting height inside the ferrite is almost identical to that of the cementite. The crack front is parallel to the $[111]_\alpha$ (or $[010]_\theta$) direction (y direction), and the propagation direction of crack is $[1\bar{1}0]_\alpha$ (or $[100]_\theta$) (x direction).

Periodic boundary conditions (PBC) are applied on the y and z directions. Free surface is generated in the x direction by introducing a vacuum layer of 50 Å, avoiding the artificial interaction between PBC images. The configuration is firstly relaxed at 0 K and zero pressure by using the conjugate gradient (cg) algorithm. After that, the interface model is given a prescribed temperature (ranging from 5 K to 300 K) and further thermally equilibrated at that targeted temperature for 200 ps with an isothermal-isobaric ensemble [60]. A Nosé-Hoover thermostat is used to control the constant temperature [61,62]. Uniaxial tension under strain control is carried out to deform the cracked model. The simulated structure is strained along the ferrite $[\bar{1}\bar{1}2]_\alpha$ direction (z axis in Fig. 1) at constant strain rates of 2×10^7, 2×10^8 s^{-1}, 2×10^9, 2×10^{10}, and 2×10^{11} s^{-1}, respectively. The other two dimensions (x and y axes in Fig. 1) are left to the condition of null stress. The MD timestep is 2 fs.

All the atomic configurations are structurally analyzed either by the common neighbor analysis (CNA) [63], or the equivalent atomic-scale shear strain [64,65] implemented in the software OVITO [66]. Details about dislocation features are further characterized by the dislocation extraction algorithm (DXA) [67].

2.2. Minimum energy pathway of dislocation nucleation

Free-end adaptive nudged elastic band (FEA-NEB) method is chosen to seek for the minimum energy path (MEP) of a dislocation activated from the ferrite-cementite interface. It is an improved version of the original free-end nudged elastic band algorithm [36] to avoid convergence problem, which can accurately locate the transition state and increase the density of images near the saddle point.

Initial and final atomic configurations for NEB calculation are obtained in the following steps. First, dislocations are introduced to the perfect ferrite-cementite interface under z-axis tensile loading at strain rate $\dot{\varepsilon} = 2.0 \times 10^8$ s^{-1} and temperature $T = 5$ K. Next, the atomic configurations at different stress levels in the elastic regime are chosen as initial configurations, while the atomic configuration with a single matured dislocation loop is chosen as the final configuration. Then, the initial and final configurations are fully relaxed by using cg algorithm.

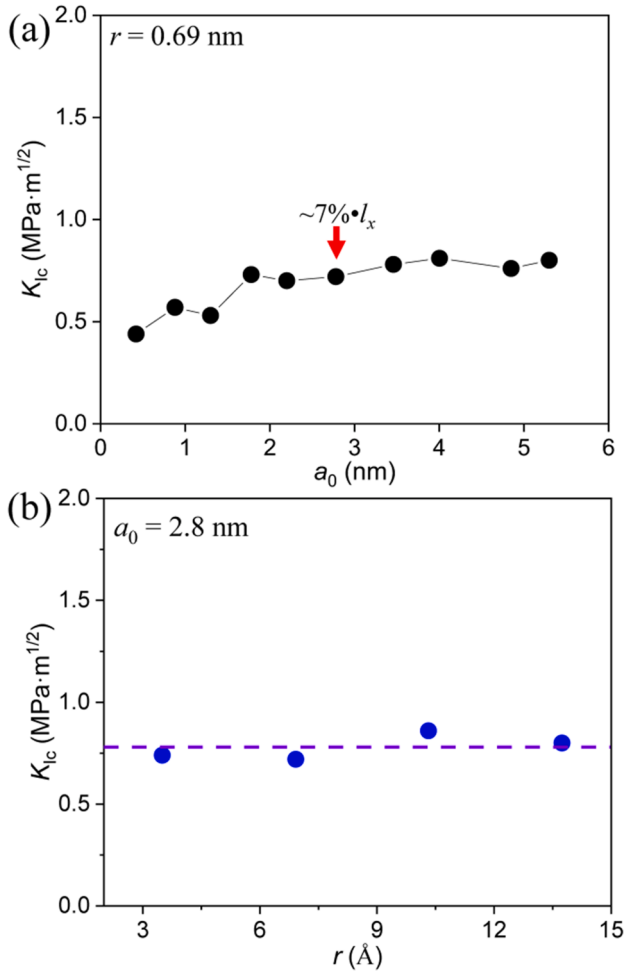

Fig. 2. Mode-I fracture toughness K_{Ic} of the ferrite-cementite interface as a function of (a) the crack half length, and (b) the crack radius at strain rate $\dot{\varepsilon} = 2 \times 10^8$ s^{-1} and temperature $T = 5$ K. Red arrow indicates the geometry of the present crack model, which is about 7% of the initial sample length in the direction of crack propagation. (For interpretation of the references to colour in this figure legend, the reader is referred to the web version of this article.)

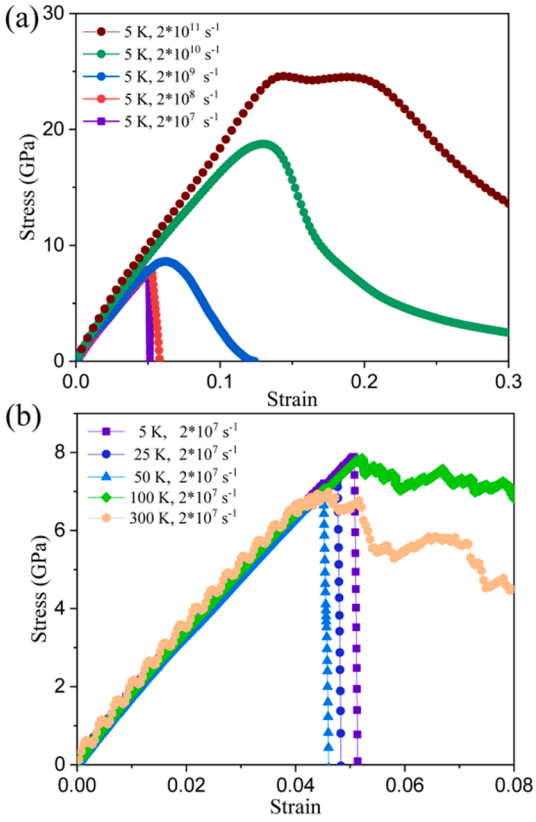

Fig. 3. Stress – strain curves of the pre-cracked ferrite-cementite interface at (a) varying strain rates and constant temperature of 5 K, and (b) varying temperatures and constant strain rate of 2×10^7 s^{-1}, for a crack with half length $a_0 = 2.8$ nm and radius $r = 0.69$ nm.

Finally, a set of intermediate images are interpolated between the two ending configurations. The images are fixed by a spring constant to constrain them along the reaction direction. It is the FEA-NEB algorithm that relaxes all the images and converges them to the MEP.

3. Results

3.1. Fracture toughness

According to the classical Griffith fracture criterion [68], brittle fracture occurs if the decrease in strain energy exceeds the increase in surface energy due to an infinitesimal crack propagation. The critical stress of the onset of crack propagation is expressed as: $\sigma_0 = \sqrt{\frac{G_c E}{\pi a_0}}$, where E is the Young's modulus, G_c the critical energy release rate, and a_0 the half length of the crack. For the present crack system, crack propagates along the ferrite-cementite interface, therefore the energy required to create two different surfaces has to be considered relative to the interfacial energy γ_{int} which gives rise to: $G_c = \gamma_\alpha + \gamma_\theta - \gamma_{int}$, here γ_α and γ_θ are the surface energies of ferrite and cementite, respectively. Considering $E = 158$ GPa and $G_c = 3.0$ J/m^2 predicted by the MEAM potential, the critical stress σ_0 is about 6.11 GPa for the half crack length $a_0 = 4.0$ nm and crack radius $r = 0.35$ nm. For comparison, the simulated critical stress is 7.50 GPa by using MD simulations, which is of the same order given by the Griffith theory. It means that the Griffith theory can be approximately applicable to depict the fracture of the ferrite-cementite interface.

Different crack half lengths (a_0) and crack radii (r) are selected to test the convergence of fracture toughness on crack geometries. The fracture toughness of mode I loading can be estimated as: $K_{Ic} = \sigma_0\sqrt{\pi a_0}$, here K_{Ic} is the critical stress intensity factor. Fig. 2 shows the simulated fracture toughness K_{Ic} of the ferrite-cementite interface with a set of pre-crack half lengths and different crack radii at $\dot{\varepsilon} = 2 \times 10^8$ s^{-1} and $T = 5$ K. With the increase in crack length, the fracture toughness first increases and then reaches a stable stage; see Fig. 2a. In contrast, Fig. 2b illustrates that the fracture toughness remains unchanged against variation in crack radius. According to the geometrical test, a combination of $a_0 = 2.8$ nm and $r = 0.69$ nm is chosen as a representative mode I crack model to further investigate the strain-rate effect on the fracture behaviors of the ferrite-cementite interface. In this case, the pre-crack length is equal to about 7% of the initial sample length along the propagation direction.

Note that the fracture toughness usually decreases with decreasing sample or grain size. Pearlitic steels with smaller interlamellar spacing (ILS) appear to be of lower fracture toughness [57,69] due to the exhaustion of mobile dislocations in the confined volume materials. It is therefore that the predicted fracture toughness of the present nanoscale pearlitic steel is about 0.8 MPa•m$^{1/2}$ with about 8 nm lamellar thickness, which is one order of magnitude smaller than the experimental value of 4 MPa•m$^{1/2}$ for the experimental sample with layer thickness about 10 nm [57]. However, the experimental sample is usually composed of much thicker ferrite phase which provides more possibility of ductile mechanisms and thus higher toughness. Consequently, it is reasonable to see that the MD data lies roughly on the extrapolation of the fracture toughness – ILS curve from the experimental samples, as shown in Fig. A1 in the Appendix.

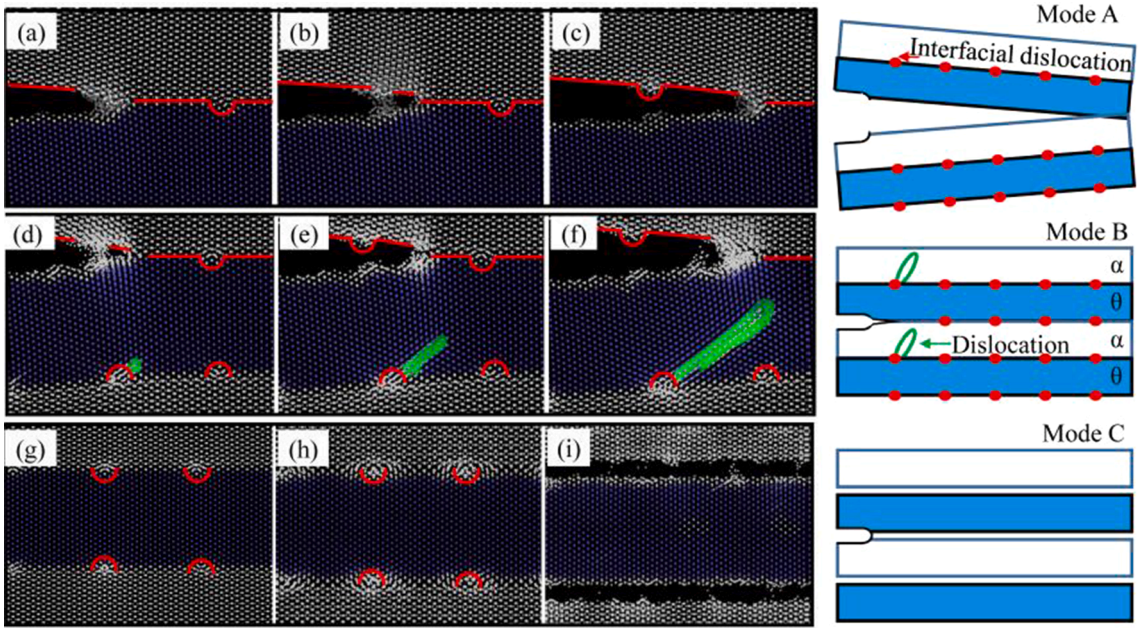

Fig. 4. Transition of three failure mechanisms with increasing strain rates at $T = 5$ K. (a)–(c) **Mode A**: brittle crack propagation along the ferrite-cementite interface, shown by the snapshots with strain magnitudes of 5.18%, 5.20%, and 5.24%, respectively, at strain rate of 2.0×10^8 s^{-1}. (b)–(f) **Mode B**: ductile dislocation nucleation in the vicinity of crack tip, illustrated by the snapshots with strains of 7.84%, 8.00%, and 8.24%, respectively, at a strain rate of 2.0×10^9 s^{-1}. (g)–(i) **Mode C**: collective delamination of the interface, demonstrated by the snapshots with strains of 4%, 20%, and 32%, respectively, at a strain rate of 2.0×10^{11} s^{-1}. Red arcs correspond to the position of the interfacial dislocations. Blue balls denote BCC atoms in ferrite. Red lines in (a)–(f) inform the propagation path of the crack. Green line in (d)–(f) denotes a $1/2\langle 111\rangle$ – type dislocation loop nucleated from the location of the interfacial dislocation. Dislocations are recognized and visualized by DXA. The right panels are cartoons of the corresponding failure mechanisms. (For interpretation of the references to colour in this figure legend, the reader is referred to the web version of this article.)

3.2. Stress – strain curves

Fig. 3 shows the stress – strain curves of the ferrite-cementite interface with a pre-crack with geometry of $a_0 = 2.8$ nm and $r = 0.69$ nm. The loading is either at different strain rates with constant temperature $T = 5$ K, or at different temperatures at constant strain rate $\dot{\varepsilon} = 2 \times 10^7$ s^{-1}. All the stress – strain curves begin with almost the same linear elastic responses. Therefore, we focus on the difference in the stress profiles after yielding. Fig. 3a shows that the peak stress at larger strain rate is higher and obviously rate-dependent, which is reasonable since plasticity is usually accommodated by stress-assisted, and thermally activated mechanisms. Similar results were reported in BCC tantalum crystal with voids [70]. For $\dot{\varepsilon} < \sim 10^9$ s^{-1}, the material fails with an abrupt stress drop, which indicates a brittle fracture with crack propagation. However, in the cases of $\dot{\varepsilon} > \sim 10^9$ s^{-1}, the stress gradually decreases after peak value, which implies the onset of possible plastic activities. This phenomenon is interesting but counterintuitive since fast loading usually leads to brittle failure. Particularly, in the case of strain rate $\dot{\varepsilon} = 2 \times 10^{11}$ s^{-1}, even a peak stress plateau exists. Note that this extreme strain rate $\dot{\varepsilon} = \sim 10^{11}$ s^{-1} is very close to the domain in which deformation are mainly controlled by lattice dynamics (athermal), where normal plastic mechanisms in crystalline structures such as crack propagation or dislocation nucleation do not exist. It thus corresponds to a certain failure mechanism with a rapid energy release. Interestingly, Fig. 3a also shows that the interface under extremely loading case ($\sim 10^{11}$ s^{-1}) has higher strength and ductility than that in relatively low loading rates.

Fig. 3b shows the effect of temperature on the stress – strain response at constant strain rate $\dot{\varepsilon} = 2 \times 10^7$ s^{-1}. For temperatures below a critical value, stress first increases elastically to a peak value and then suddenly decreases in a catastrophic way. For temperature above the critical value, obvious stress flow appears after the peak stress, which can be associated with possible plastic mechanism, e.g. dislocation nucleation at high temperatures. It indicates that there is a temperature induced brittle-to-ductile transition. In contrast with the aforementioned strain-rate-induced transition of fracture mode, the temperature effect on fracture is straightforward since thermal fluctuation encourages the onset of plastic mechanisms which would blunt the crack tip and suppress the brittle crack propagation. In a short summary, there is brittle-to-ductile transition in the ferrite-cementite interface which is stimulated by either mechanical loading or thermal fluctuation. As a result, the main aim of this study is to analyze the mechanistic and physical mechanisms underlying such an abnormal rate-induced brittle-ductile-delamination transition in the ferrite-cementite interface.

3.3. Transition of failure modes

Fig. 4 shows the three failure modes at varied strain rates emerges at $T = 5$ K. Fig. 4a – c show that crack propagates brittlely along the ferrite-cementite interface at $\dot{\varepsilon} = 2 \times 10^8$ s^{-1}, which is in agreement with experimental observation [56]. The crack propagation is damped a bit when the process meets the position of the interfacial dislocation core, where severe lattice distortion resides. We refer to this brittle crack propagation as *Mode A*. No other plastic activities are observed in the regions far away from the crack tip. It indicates a strong brittle deformation at relatively lower strain rate. In the direction of crack growth, a corrugation of local plasticity occurs in the position of interfacial dislocation due to the ductile nature of interfacial dislocations. Thus, the crack propagation proceeds in a sort of intermittent manner.

With strain rate increasing to a critical value of about 2×10^9 s^{-1}, a $1/2\langle 111\rangle$ type dislocation loop nucleates from the interface in the vicinity of crack tip, accompanied by crack blunting, as shown in Fig. 4d – f. We refer to this ductile failure involving a critical role of plastic dislocation nucleation as *Mode B*. Therefore, strain rate induces a first brittle-to-ductile transition in fracture behavior of the ferrite-cementite interface. The phenomenon is abnormal since quick loading usually brings about brittle fracture and following catastrophic failure. The mechanism will be rationalized in terms of energetic competition

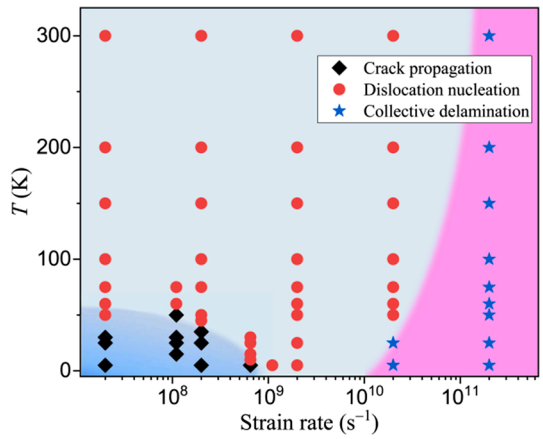

Fig. 5. Fracture diagram of the nanoscale ferrite-cementite steel in terms of strain rate and temperature. The fracture mode at any condition is judged from direct MD simulations. Transition of brittle-ductile-delamination happens as strain rate increases ($\dot{\varepsilon} \sim 10^7$ to 10^{11} s^{-1}) at different temperatures ($T \sim 5$ to 300 K).

between interface cleavage and dislocation nucleation.

A second ductile-to-brittle transition occurs by further increasing the strain rate to athermal conditions, which is corresponding to the extreme environment of shock loading. A phenomenon of the so-called collective delamination [71,72], which is defined as the instantaneous longitudinal splitting of the whole steel wire into isolated fragments with absolute and simultaneous bond breaking at all the ferrite-cementite interfaces, takes place when the strain rate increases to an extremely high value of $\sim 10^{11}$ s^{-1}. The process is demonstrated in Fig. 4 (g)−(i). We refer to this collective delamination as *Mode C*. Similar delamination was observed in the nanostructured pearlite [25] and ultrahigh-strength steel [73]. At this extreme strain rate, there is no time for either crack propagation or dislocation nucleation, only athermal process like bond breaking is allowed at the ferrite-cementite interface which is the weakest region of the material. Cartoons of the corresponding mechanisms are shown in the right panels of Fig. 4. The three distinct failure modes reported in Fig. 4 agree with the prediction from the responses of the stress − strain curves in Fig. 3a. For a first approximation, the fracture toughness K_{Ic} ($=\sigma_0\sqrt{\pi a_0}$) of collective interface delamination (Mode C), ductile dislocation nucleation (Mode B), and brittle crack propagation (Mode A) can be roughly estimated as 2.32, 0.91, and 0.73 MPa•m$^{1/2}$, respectively. In this way, the fracture mode of interface delamination has the maximum fracture toughness. The strategy of interface delamination can achieve higher fracture toughness at extremely high strain rate.

3.4. Fracture diagram

With the available information about the fracture modes, we have an opportunity to construct a two-dimensional (2D) fracture diagram of the nano-architectured ferrite-cementite pearlitic steel against strain rate and temperature, which is heuristic for the possible engineering application environment of this important structural metal. In Fig. 5 we summarize the unexpected brittle-ductile-delamination transition in fracture modes as a function of both strain rate and temperature.

In the regime of low strain rate and low temperature, brittle cleavage fracture happens with crack propagation along the ferrite-cementite interface. This is a brittle phenomenon corresponds to the successive bond breaking in front of the crack tip. The brittle crack propagation mechanism can be extrapolated to a vast regime lower strain rate cases, e.g. quasi-static loading, as evidenced by the experimentally demonstrated brittle nature of this material [56–58]. With temperature or strain rate increasing, dislocation nucleation from the ferrite-cementite interface starts to dominate the interface failure by replacing crack propagation. Dislocation emission in the vicinity of the crack tip is a thermally activated process, and it is controlled by both stress (or strain rate) and temperature [74]. Higher stress and/or temperature promote dislocation nucleation from the interface, and consequently, brittle-to-ductile transition happens in the middle regime of the fracture diagram as evidenced by the MD simulations. This ductile transition is ascribed to the competition between cleavage decohesion and dislocation nucleation at the ferrite-cementite interface. Finally, when the strain rate increases to $\sim 10^{11}$ s^{-1}, collective delamination of all the ferrite-cementite interfaces occurs, across wide temperature range. This is a completely athermal process via simultaneous delamination, in contrast with crack propagation, in the latter mode bond breaks one-by-one from crack tip to crack front with the aid of nanoscale cavitation. The fracture diagram about the abnormal brittle-ductile-delamination transition will be discussed quantitatively from a perspective of energetic competition between cleavage and dislocation nucleation in Section 4.

3.5. Atomic scale mechanism of failure modes

3.5.1. Mode A: Brittle crack propagation

Fig. 6 shows the atomic displacement field near the crack tip at different magnitudes of strain for the brittle crack propagation mechanism at $\dot{\varepsilon} = 2.0 \times 10^8$ s^{-1} and $T = 5$ K. As strain increases, the crack propagates along the ferrite-cementite interface. No dislocation nucleates from the existing interfacial dislocations. It is a manifestation of the typical brittle fracture. In addition, it is found that periodic corrugation-like fracture exists along the ferrite-cementite interface, as shown in Fig. 4a − c and 6. In general, the cleavage plane of most metallic materials is smooth [46,75,76]. The crack propagation along the ferrite-cementite interface reported in the present work is a new phenomenon. Surprisingly, the scenario of this periodic corrugation-like fracture

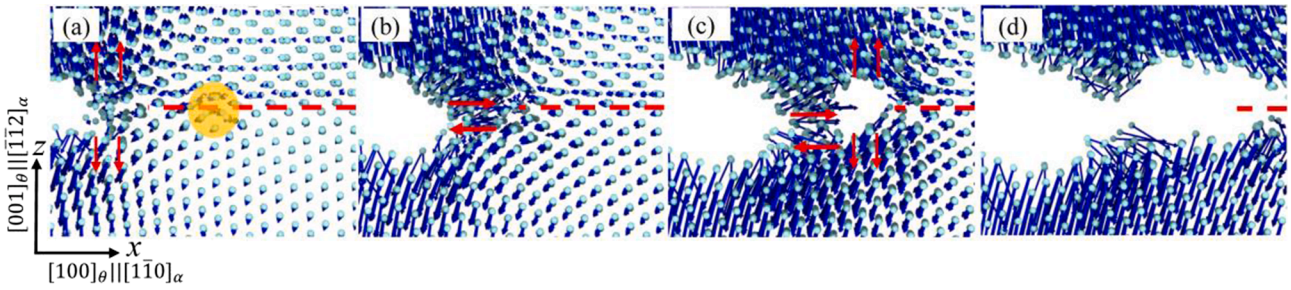

Fig. 6. Displacement map at strains of (a) 5.16%, (b) 5.18%, (c) 5.20%, and (d) 5.22% respectively, for the mechanism of brittle crack propagation at strain rate $\dot{\varepsilon} = 2.0 \times 10^8$ s^{-1} and temperature $T = 5$ K. Red horizontal dashed lines denote the position of the ferrite-cementite interface. Red arrows indicate the direction of the local stress tensor of the atoms near the crack tip. Orange circle in (a) points to the region of severe lattice distortion due to the strain field of interfacial dislocation. (For interpretation of the references to colour in this figure legend, the reader is referred to the web version of this article.)

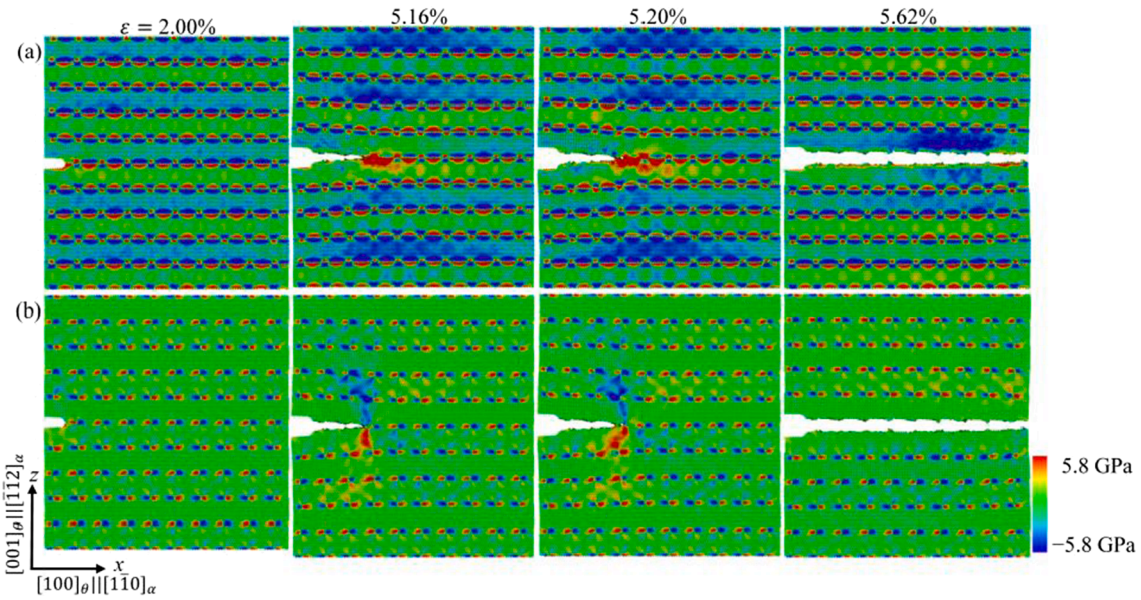

Fig. 7. Spatial distribution of atomic-level stress (a) σ_{xx} and (b) σ_{xz} at different magnitudes of strain, which is corresponding to crack propagation along the ferrite-cementite interface at strain rate $\dot{\varepsilon} = 2.0 \times 10^8\ s^{-1}$ and temperature $T = 5$ K. The atomic stresses are calculated according to virial theorem by assuming Voronoi volume of atoms.

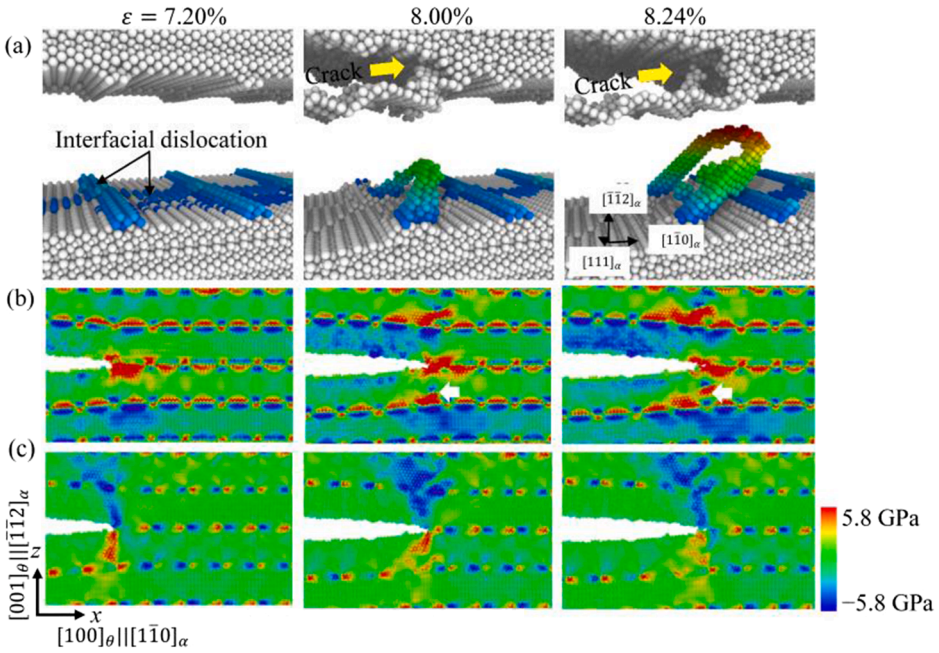

Fig. 8. Ductile fracture accommodated by dislocation nucleation from the vicinity of crack tip at strain rate $\dot{\varepsilon} = 2.0 \times 10^9\ s^{-1}$ and temperature $T = 5$ K. (a) Atomic configurations, atomic stress (b) σ_{xx}, and (c) σ_{xz} at different magnitudes of strain. Dislocation in (a) is recognized by CNA and all perfect BCC atoms have been removed for clarity. 1/2 ⟨1 1 1⟩ type dislocations nucleate in the {1 1 0} plane of ferrite. Colorful atoms in dislocation ranging from blue to red in ferrite are rendered according to their distance from the interface. Yellow arrows in (a) point to the instant position of crack tip. White arrows in (b) refer to the nucleation site of dislocation in ferrite, which is corresponding to the dislocation shown in (a). (For interpretation of the references to colour in this figure legend, the reader is referred to the web version of this article.)

mode is very similar to that in amorphous alloys or metallic glasses, in which brittle fracture is mediated by the atomic-scale cavitation [77–81]. The nanoscale periodic corrugations in amorphous alloys/metallic glasses are attributed to the formation of local softening zone ahead of crack tip, which may be related to the nature of atomic disorder characteristics of metallic glasses [77]. For crack propagation along the ferrite-cementite interface, the interfacial dislocation plays an important role in the formation of periodic corrugation. In fact, due to different lattice structures between ferrite and cementite, the periodic interfacial dislocations naturally form along the ferrite-cementite interface, as shown in Fig. 4. There is severe lattice distortion in the interfacial dislocation core, compared with the region far away from the dislocation, as orange circle shown in Fig. 6a. Consequently, locally distorted and non-distorted lattice structures are alternately arranged along the ferrite-cementite interface. When the crack meets the interfacial dislocation, atomic-scale cavitation ahead of the crack tip is first activated and the corresponding interface undergoes cleavage deformation, because the crack propagation is impeded by the strain field of interfacial dislocation with distorted lattice, as shown in Fig. 6c. The cleavage zone corresponds to relatively smooth surface, as shown in Fig. 6c and 4c. With further deformation, the coalescence of the crack and the void ahead of crack tip is generated via local dislocation-mediated plasticity, in which the atoms in the vicinity of interfacial dislocation endure shear stress. The shear coalescence position corresponds to the peak part of the corrugation. As a result, this coalescence yields a new crack tip which further propagates along the interface, as shown in Fig. 6d. The above

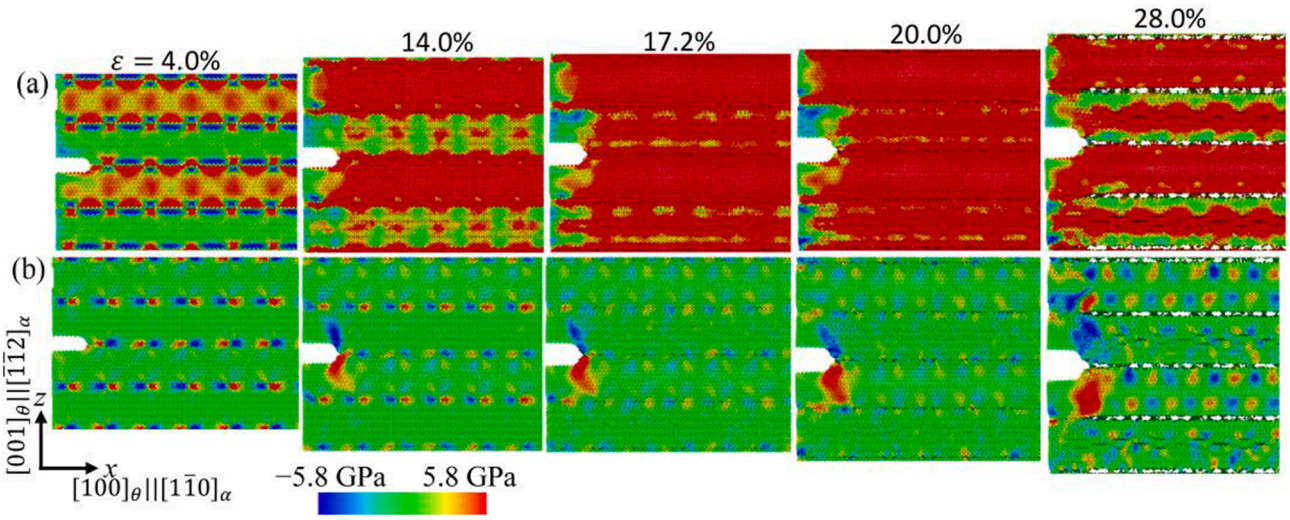

Fig. 9. Collective delamination of the ferrite-cementite interface at strain rate $\dot{\varepsilon} = 2.0 \times 10^{11}$ s^{-1} and temperature $T = 5$ K. Spatial distribution of the atomic stress (a) σ_{xx} and (b) σ_{xz} at different magnitudes of strain. Strains of 14%, 17.2%, and 20% correspond to the initial, intermediate, and complete delamination, respectively.

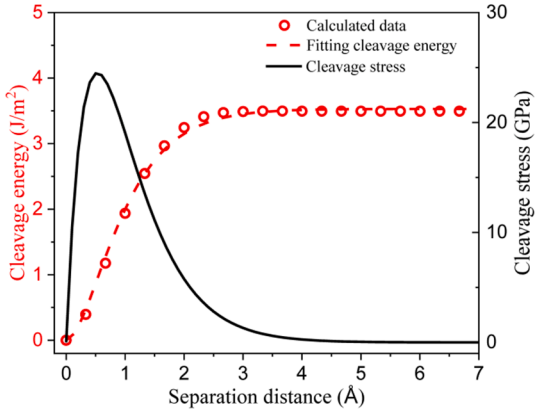

Fig. 10. Energy and stress of cleavage as a function of the separation distance for the ferrite-cementite interface. Open circles are direct MD data and dashed line is the best nonlinear fit according to Eq. (1). Solid line is stress by taking derivative of the cleavage energy per area with respect to separation distance.

combination of brittleness and local ductility will appear periodically due to the periodic arrangement of interfacial dislocations with a nanoscale separating distance, as shown in Fig. 7. In addition, most of the carbon atoms are initially located in the cementite phase, and a few carbon atoms are located in the position of the ferrite-cementite interface. Under this loading at 5 K, the carbon atoms hardly move and remain in their initial positions. Structural evolution and mechanical property changes caused by the diffusion of carbon atoms could be considered in future.

Furthermore, the spatial distribution of atomic-level stress σ_{xx} and σ_{xz} is shown in Fig. 7a and b, respectively, at different magnitudes of strain. We can notice that significant stress concentration of both σ_{xx} and σ_{xz} is observed at the crack tip, which drives the crack propagation that has to overcome the periodic obstacles of interfacial dislocation. One can also observe the symmetric distribution of absolute values of atomic stresses at the interfacial dislocation along the ferrite-cementite interface, which is periodic. This distance of periodicity is exactly equal to the interfacial dislocation spacing in the $[1\bar{1}0]_\alpha$ direction. The view from atomic-level stresses also implies rough pathway of crack propagation and the existence of intermittent motion nature of crack propagation.

3.5.2. Mode B: Ductile dislocation nucleation

Fig. 8a shows the MD snapshots of the dislocation nucleation mechanism from the interfacial interface at $\dot{\varepsilon} = 2.0 \times 10^9$ s^{-1} and $T = 5$ K. The nucleated $1/2\langle 1\,1\,1\rangle$ dislocation in ferrite is same as that reported in Ref. [33]. By comparing the configurations shown at strain magnitudes of 8.00% and 8.24% in Fig. 8a, it is concluded that the nucleated dislocation is actually the misfit dislocation embedded in the interface which bows out with the help of applied stress. This scenario is quite similar to the loop punching mechanism from precipitates having some misfit with a matrix [82,83]. The interfacial dislocation structure forms from the lattice mismatch of the two different phases, which has been demonstrated by the present authors [6] and others [1]. Upon yielding of the ferrite-cementite interface, dislocation loop starts to nucleate from the location of interfacial misfit dislocation. Afterwards, the nucleated dislocations project into the adjacent ferrite phase which is softer than cementite with lower critical resolved shear stress. The nucleated dislocations become straight lines once reaching the opposite interface. Like most experimental observations by transmission electron microscopy, dislocations spread in ferrite with the two line ends locating at the opposite interface [28]. With further crack proceeding along the ferrite-cementite interface, more plastic activities (dislocation nucleation) in ferrite are activated and it will eventually lead to crack blunting, as shown in Fig. A2 in the Appendix. Dislocation activities lead to substantial plastic deformation before fracture, which is a manifestation of ductile fracture.

Fig. 8b − c show the spatial distribution of atomic-level stress σ_{xx} and σ_{xz}, respectively, at different strains. Like the stress distribution at the case of $\dot{\varepsilon} = 2.0 \times 10^8$ s^{-1}, periodic stress arrangement along the ferrite-cementite interface is also observed. Besides crack tip, stress concentration of σ_{xx} is also noticed at the interfaces far away from the crack tip, as shown by the white arrows in Fig. 8b. It indicates the position of dislocation nucleation from the interfacial dislocation. In contrast, the stress concentration of σ_{xz} exists at crack tip at all strain levels. No distinct difference in σ_{xz} exists near the nucleated dislocations, as shown in Fig. 8c.

3.5.3. Mode C: Collective delamination

The cracked ferrite-cementite interface under extreme strain rate ($\sim 10^{11}$ s^{-1}) displays better mechanical properties, i.e. higher fracture toughness and peak stress, compared to loading cases of relatively low strain rates (shown in Fig. 3a). For this extreme loading case with higher toughness, it is found that all the ferrite-cementite interfaces delaminate at the same time. In contrast to the collective delamination mechanism

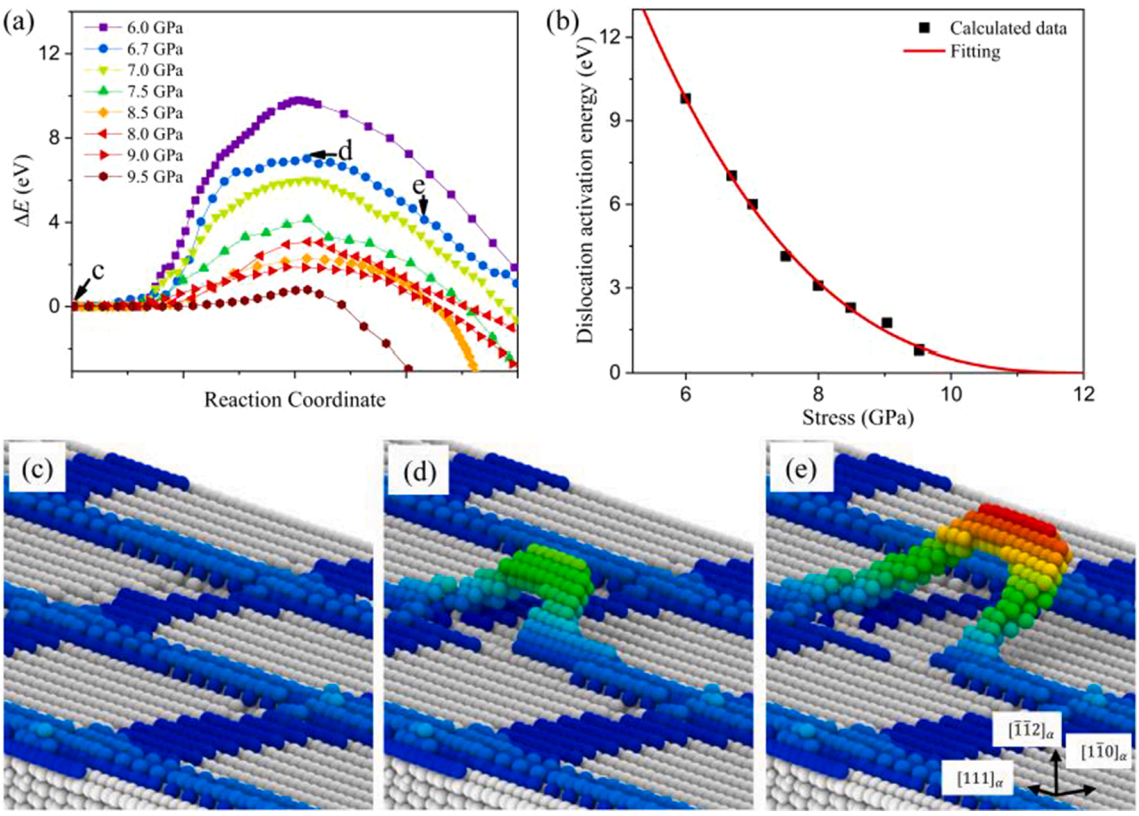

Fig. 11. (a) The minimum energy paths of dislocation nucleation at different stress levels by using FEA-NEB method [36,88]. (b) Activation energy as a function of stress. The curve is a nonlinear fit according to the Kock's law, i.e. Eq. (2). (c)–(e) Representative atomic configurations at the initial, saddle, and after-saddle states, respectively, in the case of applied stress 6.7 GPa. The corresponding positions on the nucleation path are indicated by black arrows in (a). Dislocation visualization scheme is the same as that in Fig. 8a.

for the ferrite-cementite interface under such extreme loading, this failure mechanism does not occur in pure ferrite with the same loading condition, i.e., $\dot{\varepsilon} = 2 \times 10^{11}$ s^{-1} and $T = 5$ K, as shown in Fig. A3 in Appendix. Here, the reported interface delamination is a new phenomenon in atomistic simulations of Fe-C alloys. Surprisedly, Liu *et al.* [73] recently developed a fascinating delamination toughening strategy for toughening ultrahigh-strength steels and achieved an excellent combination of ultrahigh strength and toughness by multi-grain-boundary (or interface) delamination. Their delamination toughening strategy is in good agreement with the findings in the present MD simulation in pearlitic steel. The activation of interface delamination (Mode C) requires the existence of "weak" interface [56,73].The ferrite-cementite interface can act as "weak" interface in cold-drawn pearlitic steels. Different from the atomic-level stress distribution of the loading case at $\dot{\varepsilon} = 2.0 \times 10^{9}$ s^{-1}, significant stress concentration of σ_{xx} appears in ferrite, in addition to the ferrite-cementite interfaces, at $\varepsilon = 4.0\%$ at strain rate of $\sim 10^{11}$ s^{-1}. In this elastic stage (4%), the atomic stress along the interface is periodic, as shown in Fig. 9a. When the strain increases to the end of elastic stage ($\varepsilon = 14\%$), the periodic distribution of atomic stress σ_{xx} along the interface is broken, and all atoms in the vicinity of the ferrite-cementite interface endure large tensile stress, as shown in Fig. 9. Once the tensile stress of atoms near the interface exceeds the critical stress of chemical bond breaking, the weak (or ferrite-cementite) interface is delaminated with all interfacial bond breaking. In contrast to the loading case of relatively low strain rate of $\sim 10^{8}$ s^{-1}, since the atomic stress concentration only occurs at the crack tip and the periodic distribution of atomic stress remains unchanged along interface, the atomic bonds of the interface are not broken at the same time.

The peak stress plateau of the stress – strain curve (shown in Fig. 3a) is chosen to analyze the underlying mechanism of the collective delamination. We choose the strain magnitudes of 14%, 17.2%, and 20%, which are respectively the initial, intermediate, and final stages of the peak stress plateau, to analyze the difference in atomic-level stress pattern. During this stress plateau, the interfacial distance between all the ferrite-cementite interfaces increases with increasing strain, which suggests simultaneous bond breaking, as shown in Fig. 9. At the same time, the atomic-scale stress σ_{xx} in cementite gradually increases. It means that collective delamination requires the operation of extreme large stress. The strain range (from 14% to 20%) corresponds to the process of collective delamination of all the interfaces. Once obvious delamination of the interface forms, the stress gradually releases. Strong atomic-level stress σ_{xx} reduction near the interface is observed due to the formation of new free surfaces at $\varepsilon = 28\%$, as shown in the rightmost panel of Fig. 9a. In contrast, the stress concentration of σ_{xz} only appears at crack tip at different levels of strain, as shown in Fig. 9b. While the magnitude of stress concentration increases with increasing strain, the peak stress pattern remains unchanged, which is ascribed to the formation of interface delamination which dissipates energy. At this extremely loading state, crack does not propagate along the ferrite-cementite interface, and all the interfaces are delaminated without any dislocation activities. The collective delamination (Mode C) under strain rate up to the level of $\sim 10^{11}$ s^{-1} is different from the cleavage mechanism (Mode A) which accommodates crack propagation at strain rate of $\sim 10^{8}$ s^{-1}. The former involves interface bond breakings at the same time, while the latter involves intermittent breakings of chemical bonds and is facilitated by cavitation-mediated fracture ahead of the crack tip.

4. Discussion

The aforementioned abnormal brittle-ductile-delamination transition could be deemed as a promising mechanical property that brings about new applications of pearlitic steels in extreme conditions. The fracture mode is crack propagation along the ferrite-cementite interface in the case of relatively low strain rate, and the brittle failure can be even extrapolated to quasi-static loading conditions as already shown by lots of experiments [56–58]. However, with strain rate increasing, the fracture mechanism transforms to ductile dislocation nucleation with the interfacial misfit dislocations as embryos in the vicinity of crack tip. This is a counterintuitive phenomenon. Finally, the fracture mode shifts to collective delamination of all the interfaces in the case of extremely high strain rate $\sim 10^{11}$ s^{-1}. In this section, we will discuss the possible mechanism of the brittle-ductile-delamination transition in fracture of the ferrite-cementite interface.

4.1. Cleavage energy of the ferrite-cementite interface

The universal binding-energy relation (UBER) is widely used to describe the energetics of cleavage between two adjacent atomic planes for both metallic and covalent bonding systems [84–86]. According to UBER, the cleavage energy $E_c(x)$ per interface area as a function of the interplanar separation distance can be expressed as:

$$E_c(x) = E_\infty\left\{1-\left(1+\frac{x}{\lambda}\right)\exp\left(-\frac{x}{\lambda}\right)\right\} \tag{1}$$

where λ is a characteristic length. $x = d - d_0$, here d is the separation distance between two crystal slabs under tension and d_0 is the interplanar distance in ground state. E_∞ is the energy per unit area in which the interface is thoroughly separated by an infinite distance ∞. The cleavage stress is then obtained by taking the derivative of the cleavage energy $E_c(x)$ with respect to the increment in separation distance x, which reads $\sigma_c(x) = \frac{E_\infty}{\lambda}\frac{x}{\lambda}\exp\left(-\frac{x}{\lambda}\right)$.

The cleavage energy at different separating distance can be obtained in the next steps. For a set of cleavage distance increment x, the cleavage direction normal to the ferrite-cementite interface is fixed, while the other directions in the interface plane are allowed to be relaxed by using the cg algorithm. The cleavage energy at a varied distance x is calculated by subtracting the energy of the initial perfect interface. Fig. 10 gives the calculated cleavage energy from MD simulations and the derived cleavage stress as a function of separation distance for the ferrite-cementite interface. By fitting the calculated data based on Eq. (1), we can obtain the fitting parameters $E_\infty = 3.5$ J/m^2 and $\lambda = 0.5$ Å. E_∞ is regarded as the theoretical cleavage decohesion energy of the ferrite-cementite interface, and it is equal to the energy of splitting an infinitely continuous crystal into two semi-finite halves. It thus can be expressed as: $E_\infty = \gamma_\alpha + \gamma_\theta - \gamma_{int}$. Based on this equation, the theoretical cleavage energy of 3.5 J/m^2 is in agreement with that of direct MD simulations, which predicts a value of 3.0 J/m^2. As the separation distance increases, the cleavage energy increases rapidly, and then it comes into a plateau after having been separated for $\sim$ 2.5 Å, which implies status of complete bond breaking, as shown in Fig. 10. The cleavage stress, which is derived from $E_c(x)$, has a maximum value at $x = \lambda$. This peak value of 25.3 GPa is known as the theoretical cleavage stress. It is very close to the stress required for athermal instantaneous delamination of all the interfaces, which is of 24.6 GPa as reported in Fig. 3a by MD simulations. From Fig. 10 it is judged that the cleavage energy increases with increasing stress for $x < \lambda$. Reminiscent of the scenario of decreased energy barrier with increasing stress for dislocation nucleation, the competition between the trends in two phenomena will naturally result in a crossover from crack propagation via cleavage to dislocation nucleation, if strain rate or stress keeps increasing to a hypothetical critical value.

4.2. Stress-dependent activation energy of dislocation nucleation

In order to evaluate the effect of strain rate on the energy barrier of dislocation nucleation, the activation energies of the interfacial dislocation nucleation are estimated quantitatively at different magnitudes of applied uniaxial tensile stress. Fig. 11a shows the MEPs of dislocation nucleation at different stresses by using FEA-NEB method. As expected, the energy barrier corresponding to dislocation nucleation becomes lower at higher stress. The maximum energy in the MEP over the potential energy of the initial configuration is defined as the activation energy of dislocation nucleation. All the calculated activation energies of dislocation nucleation at different stresses are summarized in Fig. 11b. A well accepted Kock's law [87] is then used to fit the set of the evaluated data points. The Kock's law is expressed as:

$$Q(\sigma) = Q_0\left(1-\frac{\sigma}{\sigma_{ath}}\right)^q \tag{2}$$

where $Q(\sigma)$ and Q_0 are the activation energies at an applied stress σ and null stress, respectively. σ_{ath} is the athermal stress which sets up an upper limit of possible critical stress for dislocation nucleation. Q_0, σ_{ath}, and q are fitting parameters in this scheme. The red line in Fig. 11b is the fitting curve based on Eq. (2) by taking $\sigma_{ath} = 12.2$ GPa, which is approximated by the critical stress of dislocation nucleation estimated by MD at $\dot{\varepsilon} = 2.0 \times 10^8$ s^{-1} and $T = 5$ K. The fitting parameters $Q_0 = 68.5$ eV and $q = 2.9$, respectively. The corresponding coefficient of determination is 0.997, which indicates the fit is satisfactory with the present set of parameters.

For an intuitive understanding of the dislocation nucleation mechanism, we further demonstrate the MEP in the case of typical stress condition 6.7 GPa. The atomic configurations of the initial, saddle, and after-saddle points are displayed in Fig. 11c – e. It is clearly visible that an original interfacial dislocation is bowed out from the interface and forms a dislocation embryo. The embryo further grows into a matured dislocation loop and then enters into the ferrite phase with the help of applied stress. The activated 1/2 ⟨1 1 1⟩ dislocation by using FEA-NEB method is consistent with that nucleated under tensile loadings, as shown in Fig. 8a – c. The mechanism informed by FEA-NEB reproduces well the dislocation operations under monotonic deformation, which has been also reported in previous MD simulations [25,33].

4.3. Rationalization of the brittle-ductile-delamination transition

The brittle-to-ductile transition is attributed to the competition between cleavage and dislocation nucleation at the ferrite-cementite interface. As shown in Section 4.1, the theoretical cleavage energy is calculated as a constant value, which is almost independent on the stress level. In contrast, the energy of dislocation nucleation from the ferrite-cementite interface decreases with the increases of stress (or strain rate), as shown in Fig. 11. In this way, there will be a critical strain rate between the brittle crack propagation via cleavage and the ductile crack blunting accommodated by dislocation nucleation. Brittle cleavage with crack propagation along the ferrite-cementite interface takes place for stress below the critical value. When stress exceeds the critical value, a clear transition from cleavage to dislocation nucleation occurs. With further stress increasing, dislocation nucleation starts to dominate the cracking behavior due to lower energy needed at the same stress level. This indicates that strain rate is capable to induce ductile dislocation nucleation from the ferrite-cementite interface, in contrast with the usual idea of a unique fracture mode in the whole high-strain-rate domain, such as the shock loading conditions. A critical strain rate of the brittle-to-ductile transition will be determined in our near future.

We have discussed the mechanistic mechanism of the first brittle-to-ductile transition from a perspective of competition between the cleavage energy of interface and the activation energy of dislocation nucleation. Thermal-activated dislocation nucleation can be accelerated

by high stress and temperature. Higher stress (due to high strain rate) reduces the activation energy for dislocation nucleation and, thus, increases the rate of such events. In contrast, cleavage with participation of successive bonding breaking is sort of an athermal process, and the cleavage energy is much less related to strain rate.

While both the two transitions are not reported in literature, the second ductile-to-delamination transition from thermally activated dislocation nucleation to athermal delamination is understood. In the case of athermal loading, there is no enough time for either crack propagation, or dislocation initiation, both of which involves critical role of phonon propagation. In the case of instantaneous delamination at the interface, only quick breaking of weak bond is necessitated at extremely short time, in contrast to break any strong bonds in the bulk regions. Once the local tensile stress of atoms near the interface exceeds the critical stress of chemical bond breaking (of that specific atomic environment), the weak ferrite-cementite interface is delaminated with all instantaneous interfacial bond breaking. Higher strain rate leads to higher stress, and the critical stress drives bond breaking. Thus, there should be a failure criterion based on MEAM potential, which is constructed from the strain rate and other physical variables associated with different bonding nature, controlling over whether the ferrite-cementite interface fails in a ductile manner or collective delamination. When loading strain rate is less than the critical strain rate, the interface fails in a ductile dislocation manner. Once strain rate exceeds the critical value, the interface failure transforms from a ductile manner to the collective delamination. The above failure criterion based on strain rate strongly depend on atomic interaction potential and, thus, the specific bonding nature at the interface. The correlation between the critical strain rate and the bond breaking nature deserves furthermore study in future work.

5. Conclusion

In summary, extensive atomistic simulations uncover strain-rate-induced abnormal brittle-ductile-delamination transition in the fracture behaviors of a nanoscale ferrite-cementite cold-drawn pearlitic steel under mode I loading. MD simulations report fracture toughness of ferrite-cementite steel in line with the prediction from experiments. With strain rate increasing, the failure mode transforms from brittle crack propagation to ductile dislocation nucleation, and, finally, to collective delamination of all interfaces at extremely high strain rate. At relatively low strain rate below $\sim 10^8\ s^{-1}$, brittle crack propagates along the ferrite-cementite interface via intermittent interface cleavage. This crack propagation along the interface is in agreement with experimental observation at quasi-static loading. This brittle mechanism is mediated by nanoscale cavitation in front of the crack tip. At middle strain rate domain of $\sim 10^9\ s^{-1}$, ductile dislocations start to bow out from the interface and slip into the ferrite phase. Therefore, ductile mode governs fracture and produces a brittle-to-ductile transition with increasing strain rate. At extremely high strain rate of $\sim 10^{11}\ s^{-1}$, collective delamination of all the ferrite-cementite interfaces occurs. The deformation is so quick that neither crack propagation nor dislocation nucleation is allowed, since both two mechanisms involve participation of phonon propagation, which is of time scale picosecond that is already comparable to loading rate.

Informed by the MD reported fracture modes, we have established a failure fracture mechanism diagram of the ferrite-cementite steel with respect to strain rate and temperature. The brittle-to-ductile transition is attributed to the energetic competition between cleavage and dislocation nucleation. Once the applied stress strain rate is higher than the critical value, the plastic dislocation nucleation starts to dominate the cracking of the ferrite-cementite interface. The second transition from dislocation nucleation to collective delamination is accommodated by the thermal to athermal loading. In the latter case, extremely high stress provided by high strain rate reaches the level of bond breaking stress, and no mechanism other than the sudden delamination of interface is necessary. The present atomistic simulations combined with possible mechanistic model provide microscopic insight to the abnormal brittle-ductile-delamination transition in fracture modes, which sheds light on coordinating applications of the high-strength cold-drawn pearlitic steels in extreme environments.

Data availability

The data required to reproduce these findings cannot be shared at this time due to technical or time limitations but will be available upon reasonable request.

Declaration of Competing Interest

The authors declare that they have no known competing financial interests or personal relationships that could have appeared to influence the work reported in this paper.

Data availability

Data will be made available on request.

Acknowledgments

The NSFC Basic Science Center Program for “Multiscale Problems in Nonlinear Mechanics” (No.11988102), the NSFC (No. 11790292, No. 11972346, and No. 12072344), the Strategic Priority Research Program (No. XDB22040302 and No. XDB22040303), the Key Research Program of Frontier Sciences (Grant No. QYZDJSSW-JSC011), Science Challenge Project (No. TZ2016001), and the Youth Innovation Promotion Association (No. 2017025) of the Chinese Academy of Sciences, the opening project of State Key Laboratory of Explosion Science and Technology (Beijing Institute of Technology, No. KFJJ18-14M). All the calculations were performed on the “Era” petascale supercomputer of the Computer Network Information Center of CAS.

Appendix

A.1. Fracture toughness of MD versus experimental values

See Fig. A1.

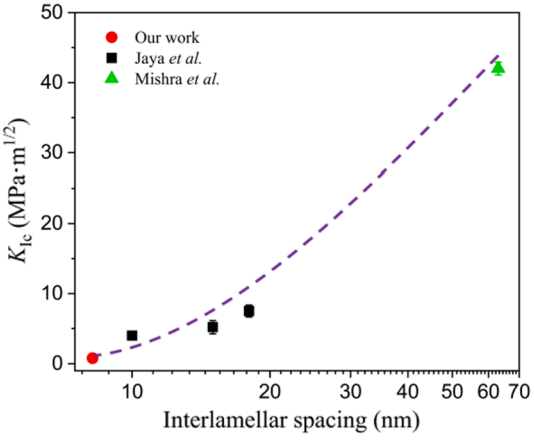

Fig. A1. Comparison in fracture toughness K_{Ic} of MD simulations with experimental values for the cold-drawn pearlitic steels as a function of the ferrite-cementite interlamellar spacing. Circle is the present MD data. Rectangles and triangle are the experimental data from Refs. [57] and [69], respectively. It is noticed that MD data falls in the scope of the predictions from extrapolation of experimental measurements. The dashed curve serves as guide to the eye.

A.2. Atomic-level strain pattern for mode B: dislocation nucleation

See Fig. A2.

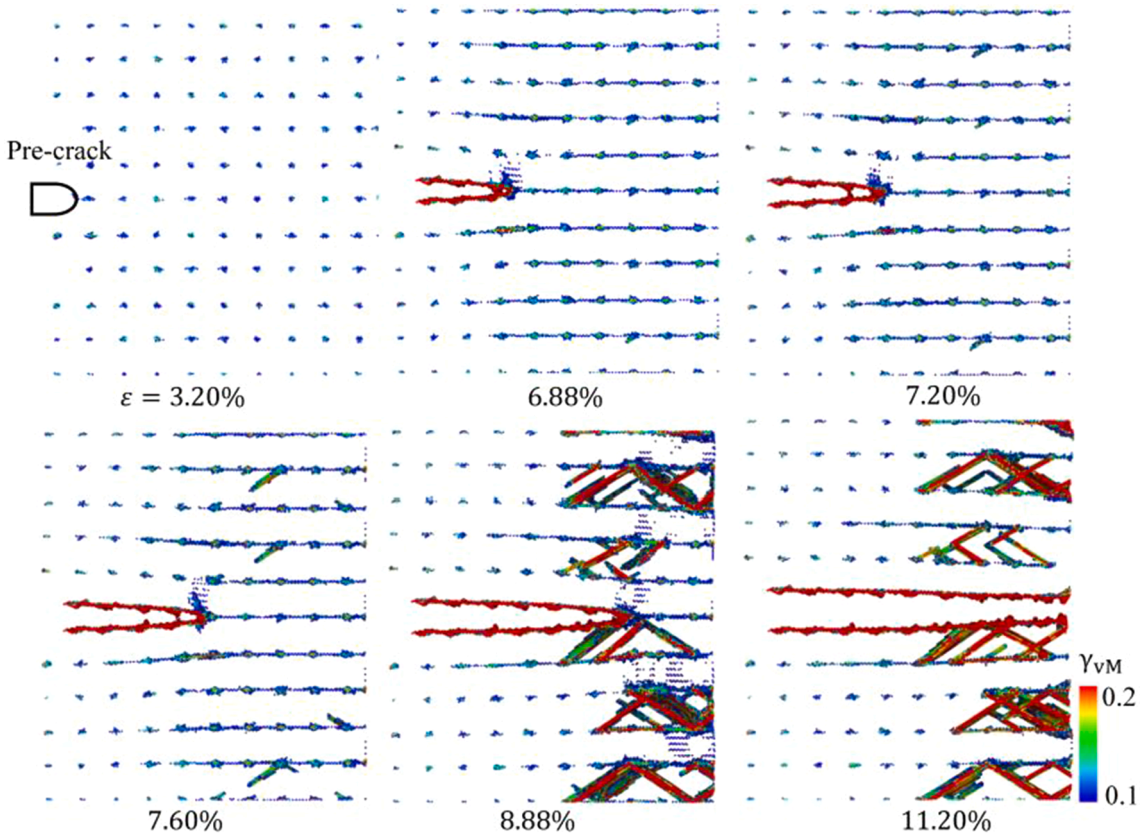

Fig. A2. Distribution of the atomic-level von Mises equivalent shear strain in the pre-cracked model of the ferrite-cementite interface at different magnitudes of strain with loading condition $\dot{\varepsilon} = 2 \times 10^9$ s^{-1} and $T = 5$ K. All the atoms with von Mises strain less than 0.1 are removed for clarity. Crack blunts by the dislocation nucleation in the vicinity of crack tip.

A.3. Atomic-level strain pattern for pure ferrite

See Fig. A3.

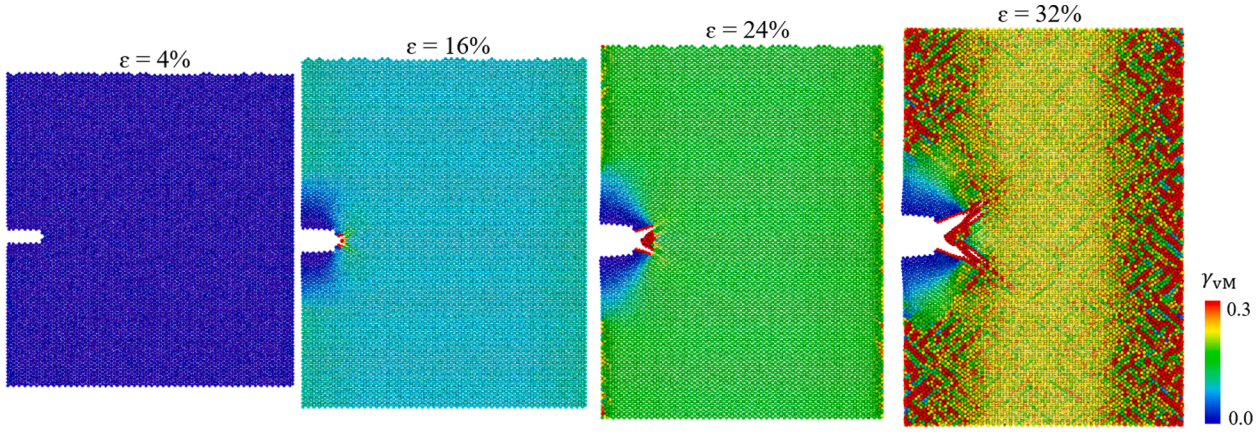

Fig. A3. Distribution of the atomic-level von Mises equivalent shear strain in the pre-cracked model of pure ferrite at different magnitudes of strain with loading condition $\dot{\varepsilon} = 2 \times 10^{11}$ s^{-1} and $T = 5$ K. No delamination occurs in iron under such extreme loading case.

References

[1] C. Borchers, R. Kirchheim, Prog. Mater Sci. 82 (2016) 405–444.
[2] Y. Li, D. Raabe, M. Herbig, P.-P. Choi, S. Goto, A. Kostka, H. Yarita, C. Borchers, R. Kirchheim, Phys. Rev. Lett. 113 (2014), 106104.
[3] X. Zhang, N. Hansen, A. Godfrey, X. Huang, Acta Mater. 114 (2016) 176–183.
[4] T. Junge, J.-F. Molinari, Int. J. Plast. 53 (2014) 90–106.
[5] F. Zhou, J.-F. Molinari, Y. Li, Eng. Fract. Mech. 71 (2004) 1357–1378.
[6] D. Wei, L. Wang, X. Hu, X. Mao, Z. Xie, F. Fang, J. Mater. Sci. (2022) 1–16.
[7] J. Langer, E. Bouchbinder, T. Lookman, Acta Mater. 58 (2010) 3718–3732.
[8] D.L. Tonks, in, Los Alamos National Laboratory Report No. LA 12641, 1993.
[9] M.A. Meyers, Dynamic behavior of materials, John wiley & sons, 1994.
[10] R. Armstrong, Mater. Sci. Eng. 1 (1966) 251–254.
[11] J.R. Rice, R. Thomson, Philos. Mag. 29 (1974) 73–97.
[12] V. Podgurschi, D.J.M. King, K. Luo, M.R. Wenman, Comput. Mater. Sci. 206 (2022), 111220.
[13] G. Xu, A.S. Argon, M. Ortiz, Philos. Mag. A 72 (1995) 415–451.
[14] I.A. Bryukhanov, A.V. Larin, J. Appl. Phys. 120 (2016), 235106.
[15] Z. Xing, H. Fan, G. Kang, Comput. Mater. Sci. 210 (2022), 111058.
[16] Z. Zhao, Z. Qin, F. Chu, Comput. Mater. Sci. 158 (2019) 178–191.
[17] J.R. Rice, J. Mech. Phys. Solids 40 (1992) 239–271.
[18] Y. Zhang, F.-C. Zhang, L.-H. Qian, T.-S. Wang, Comput. Mater. Sci. 50 (2011) 1754–1762.
[19] S.-P. Jung, Y. Kwon, C.S. Lee, B.-J. Lee, Comput. Mater. Sci. 149 (2018) 424–434.
[20] T. Sirithanakorn, M. Tanaka, K. Higashida, Mater. Sci. Eng. A 611 (2014) 383–387.
[21] T. Sirithanakorn, M. Tanaka, K. Higashida, Adv. Mater. Res. 922 (2014) 706–710.
[22] J. Wang, A. Misra, Curr. Opin. Solid State Mater. Sci. 15 (2011) 20–28.
[23] D. Wei, X. Min, X. Hu, Z. Xie, F. Fang, Mater. Sci. Eng. A 784 (2020), 139341.
[24] T. Shimokawa, T. Niiyama, M. Okabe, J. Sawakoshi, Acta Mater. 164 (2019) 602–617.
[25] M. Guziewski, S.P. Coleman, C.R. Weinberger, Acta Mater. 180 (2019) 287–300.
[26] L.-W. Liang, Y.-J. Wang, Y. Chen, H.-Y. Wang, L.-H. Dai, Acta Mater. 186 (2020) 267–277.
[27] Y.J. Li, P. Choi, C. Borchers, Y.Z. Chen, S. Goto, D. Raabe, R. Kirchheim, Ultramicroscopy 111 (2011) 628–632.
[28] X. Zhang, A. Godfrey, X. Huang, N. Hansen, Q. Liu, Acta Mater. 59 (2011) 3422–3430.
[29] J. Kim, K. Kang, S. Ryu, Int. J. Plast. 83 (2016) 302–312.
[30] H. Ghaffarian, A.K. Taheri, K. Kang, S. Ryu, Multiscale Sci. Eng. 1 (2019) 47–55.
[31] R.K. Barik, A. Ghosh, S.M. Basiruddin, S. Biswal, A. Dutta, D. Chakrabarti, Acta Mater. 214 (2021), 116988.
[32] Z. Qi, L. He, F. Wang, J. Wang, J. Cheng, G. Xie, X. Zeng, Mech. Mater. 165 (2022), 104185.
[33] M. Guziewski, S.P. Coleman, C.R. Weinberger, Acta Mater. 144 (2018) 656–665.
[34] X. Li, Y. Wei, L. Lu, K. Lu, H. Gao, Nature 464 (2010) 877–880.
[35] K. Lu, L. Lu, S. Suresh, Science 324 (2009) 349–352.
[36] T. Zhu, J. Li, A. Samanta, H.G. Kim, S. Suresh, Proc. Natl. Acad. Sci. U S A, 104 (2007) 3031-3036.
[37] G. Sainath, B.K. Choudhary, T. Jayakumar, Comput. Mater. Sci. 104 (2015) 76–83.
[38] Y.-F. Guo, Y.-S. Wang, D.-L. Zhao, Acta Mater. 55 (2007) 401–407.
[39] Y.-F. Guo, Y.-S. Wang, D.-L. Zhao, W.-P. Wu, Acta Mater. 55 (2007) 6634–6641.
[40] J.J. Möller, E. Bitzek, Modell. Simul. Mater. Sci. Eng. 22 (2014), 045002.
[41] Z. Wang, X. Shi, X.-S. Yang, W. He, S.-Q. Shi, X. Ma, J. Mater. Sci. 56 (2021) 2275–2295.
[42] C.H. Ersland, I.R. Vatne, C. Thaulow, Modell. Simul. Mater. Sci. Eng. 20 (2012), 075004.
[43] P.A. Gordon, T. Neeraj, M.J. Luton, Modell. Simul. Mater. Sci. Eng. 16 (2008), 045006.
[44] T. Zhu, J. Li, S. Yip, Phys. Rev. Lett. 93 (2004), 205504.
[45] Y. Cheng, Z.H. Jin, Y.W. Zhang, H. Gao, Acta Mater. 58 (2010) 2293–2299.
[46] J.J. Möller, E. Bitzek, Acta Mater. 73 (2014) 1–11.
[47] S. Plimpton, J. Comput. Phys. 117 (1995) 1–19.
[48] L.S. Liyanage, S.-G. Kim, J. Houze, S. Kim, M.A. Tschopp, M.I. Baskes, M. F. Horstemeyer, Phys. Rev. B 89 (2014), 094102.
[49] K.O. Henriksson, K. Nordlund, Phys. Rev. B 79 (2009), 144107.
[50] D.J. Hepburn, G.J. Ackland, Phys. Rev. B 78 (2008), 165115.
[51] M. Guziewski, S.P. Coleman, C.R. Weinberger, Acta Mater. 119 (2016) 184–192.
[52] L. Xiang, L. Liang, Y. Wang, Y. Chen, H. Wang, L. Dai, Mater. Sci. Eng. A 757 (2019) 1–13.
[53] D. Zhou, G. Shiflet, Metall. Trans. A 23 (1992) 1259–1269.
[54] M.-X. Zhang, P. Kelly, Scr. Mater. 37 (1997) 2009–2015.
[55] Y.A. Bagaryatskii, G. Nosova, T. Tagunova, Dokl. Akad. Nauk SSSR 105 (1955) 1225.
[56] A. Hohenwarter, B. Voelker, M.W. Kapp, Y. Li, S. Goto, D. Raabe, R. Pippan, Sci. Rep. 6 (2016) 33228.
[57] B.N. Jaya, S. Goto, G. Richter, C. Kirchlechner, G. Dehm, Mater. Sci. Eng. A 707 (2017) 164–171.
[58] T. Leitner, S. Sackl, B. Voelker, H. Riedl, H. Clemens, R. Pippan, A. Hohenwarter, Scripta Mater. 142 (2018) 66–69.
[59] K.O.E. Henriksson, C. Björkas, K. Nordlund, J. Phys.: Condens. Matter 25 (2013), 445401.
[60] M. Parrinello, A. Rahman, J. Appl. Phys. 52 (1981) 7182–7190.
[61] S. Nosé, Mol. Phys. 52 (1984) 255–268.
[62] W.G. Hoover, Phys. Rev. A 31 (1985) 1695–1697.
[63] J.D. Honeycutt, H.C. Andersen, J. Phys. Chem. 91 (1987) 4950–4963.
[64] M.L. Falk, J.S. Langer, Phys. Rev. E 57 (1998) 7192–7205.
[65] F. Shimizu, S. Ogata, J. Li, Mater. Trans. 48 (2007) 2923–2927.
[66] A. Stukowski, Modell. Simul. Mater. Sci. Eng. 18 (2010), 015012.
[67] A. Stukowski, V.V. Bulatov, A. Arsenlis, Modell. Simul. Mater. Sci. Eng. 20 (2012), 085007.
[68] A.A. Griffith, Philos, Trans. R. Soc. Lond. Ser. A 221 (1921) 163–198.
[69] K. Mishra, A. Singh, Mater. Sci. Eng. A 706 (2017) 22–26.
[70] L.A. Zepeda-Ruiz, A. Stukowski, T. Oppelstrup, V.V. Bulatov, Nature 550 (2017) 492–495.
[71] C.M. Bae, W.J. Nam, C.S. Lee, Scripta Mater. 35 (1996) 641–646.
[72] L. Zhou, F. Fang, L. Wang, H. Chen, Z. Xie, J. Jiang, Mater. Sci. Eng. A 713 (2018) 52–60.
[73] L. Liu, Q. Yu, Z. Wang, J. Ell, M.X. Huang, R.O. Ritchie, Science 368 (2020) 1347–1352.
[74] A. Evans, R. Rawlings, Phys. Stat. Sol. 34 (1969) 9–31.
[75] D. Jang, X. Li, H. Gao, J.R. Greer, Nat. Nanotechnol. 7 (2012) 594–601.
[76] Y.J. Wang, K. Tsuchiya, L.H. Dai, Mater. Sci. Eng. A 649 (2016) 449–460.
[77] M.Q. Jiang, Z. Ling, J.X. Meng, L.H. Dai, Philos. Mag. 88 (2008) 407–426.
[78] P. Murali, T.F. Guo, Y.W. Zhang, R. Narasimhan, Y. Li, H.J. Gao, Phys. Rev. Lett. 107 (2011), 215501.
[79] Y. Chen, M.Q. Jiang, Y.J. Wei, L.H. Dai, Philos. Mag. 91 (2011) 4536–4554.
[80] X. Huang, Z. Ling, L.H. Dai, Int. J. Solids Struct. 50 (2013) 1364–1372.
[81] L.-Q. Shen, J.-H. Yu, X.-C. Tang, B.-A. Sun, Y.-H. Liu, H.-Y. Bai, W.-H. Wang, Sci. Adv. 7 (2021).
[82] H. Xie, K. Xu, G.-H. Lu, T. Yu, F. Yin, Scripta Mater. 147 (2018) 98–102.
[83] G.W. Greenwood, A.J.E. Foreman, D.E. Rimmer, J. Nucl. Mater. 1 (1959) 305–324.
[84] J.H. Rose, J.R. Smith, F. Guinea, J. Ferrante, Phys. Rev. B 29 (1984) 2963–2969.
[85] A. Srirangarajan, A. Datta, A.N. Gandi, U. Ramamurty, U.V. Waghmare, J. Phys.: Condens. Matter 26 (2014), 055006.
[86] H. Gholizadeh, S. Hasani, Comput. Mater. Sci. 143 (2018) 515–527.
[87] U.F. Kocks, A.S. Argon, M.F. Ashby, Prog. Mater Sci. 19 (1975) 1–281.
[88] J. Zhang, H. Zhang, H. Ye, Y. Zheng, J. Chem. Phys. 145 (2016), 094104.